Layer Hall Detection of the Néel Vector in Centrosymmetric Magnetoelectric Antiferromagnets

L. L. Tao,[1,*] Qin Zhang,[1] Huinan Li,[1] Hong Jian Zhao,[2,3,†] Xianjie Wang,[1] Bo Song,[4] Evgeny Y. Tsymbal,[5] and Laurent Bellaiche[6,7]

[1]*School of Physics, Harbin Institute of Technology, Harbin 150001, China*
[2]*Key Laboratory of Material Simulation Methods and Software of Ministry of Education, College of Physics, Jilin University, Changchun 130012, China*
[3]*International Center of Future Science, Jilin University, Changchun 130012, China*
[4]*National Key Laboratory of Science and Technology on Advanced Composites in Special Environments, Harbin Institute of Technology, Harbin 150001, China*
[5]*Department of Physics and Astronomy & Nebraska Center for Materials and Nanoscience, University of Nebraska, Lincoln, Nebraska 68588-0299, USA*
[6]*Smart Ferroic Materials Center, Physics Department and Institute for Nanoscience and Engineering, University of Arkansas, Fayetteville, Arkansas 72701, USA*
[7]*Department of Materials Science and Engineering, Tel Aviv University, Ramat Aviv, Tel Aviv 6997801, Israel*

(Received 15 November 2023; accepted 23 July 2024; published 30 August 2024)

The efficient detection of the Néel vector in antiferromagnets is one of the prerequisites toward antiferromagnetic spintronic devices and remains a challenging problem. Here, we propose that the layer Hall effect can be used to efficiently detect the Néel vector in centrosymmetric magnetoelectric antiferromagnets. Thanks to the robust surface magnetization of magnetoelectric antiferromagnets, the combination of sizable exchange field and an applied electric field results in the layer-locked spin-polarized band edges. Moreover, the Berry curvature can be engineered efficiently by an electric field, which consequently gives rise to the layer-locked Berry curvature responsible for the layer Hall effect. Importantly, it is demonstrated that the layer Hall conductivity strongly depends on the Néel vector orientation and exhibits rich electromagnetic responses, which can be used to detect the Néel vector reversal. Based on density functional theory calculations, we exemplify those phenomena in the prototypical Cr_2O_3 compound. A complete list of the magnetic point groups sustaining the layer Hall effect is presented, aiding the search for realistic materials. Our work proposes a novel approach to detect the Néel vector and holds great promise for antiferromagnetic spintronic applications.

DOI: 10.1103/PhysRevLett.133.096803

Introduction—Antiferromagnetic spintronics rooted in antiferromagnets (AFMs) have aroused considerable interest since the last decade due to the attractive properties of AFMs such as zero stray fields, ultrafast dynamics, and robustness against magnetic perturbations [1–5]. The antiferromagnetic order parameter known as Néel vector could serve as a nonvolatile variable to design the promising antiferromagnetic memory device [2,3]. In this regard, the efficient detection of the Néel vector becomes one of the basic principles enabling such device design [2–5]. In contrast to ferromagnets, the lack of sizable magnetization makes it technically nontrivial to detect the Néel vector in AFMs (readout of the AFM state) using conventional magnetic techniques. Recently, several approaches such as anisotropic magnetoresistance (AMR) [6,7], spin Hall magnetoresistance [8,9], magneto-optical Kerr [4,10,11], *extrinsic* [12–14] and *intrinsic* nonlinear Hall effect (NHE) [15–17] have been proposed to detect the Néel vector. Despite these advances, these approaches are merely applicable to a special class of AFMs and have their own limitations. For example, the magneto-optical Kerr is mostly valid for canted AFMs with weak ferromagnetism [11]. The AMR and *extrinsic* NHE cannot distinguish a 180° reversal of the Néel vector [14–16]. In this regard, the techniques for the Néel vector detection in AFMs are far from complete, and proposals of novel detection schemes are highly desirable.

In this Letter, we propose that the layer Hall effect [18] represents an efficient tool to detect the Néel vector of $\mathcal{PT}$-symmetric ($\mathcal{P}$ denotes inversion while $\mathcal{T}$ denotes time reversal) magnetoelectric (ME) AFMs, owing to their following advantages. First, the $\mathcal{PT}$-symmetric AFMs enable the control of the Néel vector via fieldlike

[*]Contact author: lltao@hit.edu.cn
[†]Contact author: physzhaohj@jlu.edu.cn

spin-orbit torque [6,10,19,20] and, as shall be shown, the electrically switchable Hall signal. Second, the ME AFMs [21–23] are attractive due to possessing an intrinsic ME effect and roughness-robust surface magnetization $\mathcal{M}$, which is protected by bulk magnetic symmetries [24–27]. Specifically, the vacuum-terminated surface or interface with another material reduces the bulk magnetic point group in a similar way as electric field does. Thus, the same equilibrium magnetization components as the bulk magnetoelectric with an applied electric field must exist at the boundary [26,27]. Strikingly, $\mathcal{M}$ tied to the bulk Néel vector is ME switchable [8,25,28]. This offers a desirable route for the Néel vector detection through examining $\mathcal{M}$-dependent physical responses. Recently, a new type of Hall effect—the layer Hall effect—was proposed and experimentally observed in the 2D topological axion antiferromagnet $MnBi_2Te_4$ [18]. Such layer Hall effect is distinct from the conventional anomalous Hall effect (AHE) and originates from the layer-locked Berry curvature, namely the Berry curvatures are opposite between the top and bottom layers [29,30]. Since the layer Hall effect is a layer-locked AHE and $\mathcal{M}$ is locked to the surface layer, it is instructive to explore the layer Hall effect and its dependence on the Néel vector orientation in ME AFMs. Here, we predict that the layer Hall effect emerges in the centrosymmetric ME AFM when an electric field is applied. As a specific example, we consider the prototypical ME AFM Cr_2O_3 and demonstrate a sizable layer Hall signal based on the density functional theory calculations. Moreover, we show that the layer Hall conductivity depends strongly on the Néel vector orientation, which suggests an efficient way to detect the Néel vector.

Layer Hall effect from symmetry analysis—We first illustrate the strategy for fulfilling the layer Hall effect in centrosymmetric ME AFMs from symmetry analysis. For centrosymmetric ME AFMs [31], both $\mathcal{P}$ and $\mathcal{T}$ symmetries are broken while the combined $\mathcal{PT}$ symmetry is preserved. As sketched in Fig. 1(a), the ME AFM film contains two symmetrically equivalent surfaces (termed as the top and bottom layers connected by $\mathcal{PT}$ symmetry) with opposite $\mathcal{M}$. $\mathcal{M}$ is protected by the symmetry operation $\{R|\mathbf{t}\}$ [26,27], where R and $\mathbf{t}$ denote the point group and translation operations, respectively. From Fig. 1(a), although $\mathbf{t}$ creates atomic steps at the surface, both $\mathcal{M}$ and surface normal $\mathbf{n}$ are invariant under R operation, thereby generating uncompensated $\mathcal{M}$. The exchange field produced by $\mathcal{M}$ [32–34] yields a sizable exchange splitting Δ_1 between $t_\uparrow$ and $t_\downarrow$ ($b_\uparrow$ and $b_\downarrow$) energy levels, where $\uparrow, \downarrow$ is the spin index and t (b) denotes the state associated with the top (bottom) layer. To examine the bands and Berry curvature engineering by an applied electric field, without loss of generality, we consider $\mathbf{n}$ along z direction in the following discussion. Without electric field E_z, the global $\mathcal{PT}$ symmetry ensures the Kramers degeneracy and the vanishing Berry curvature

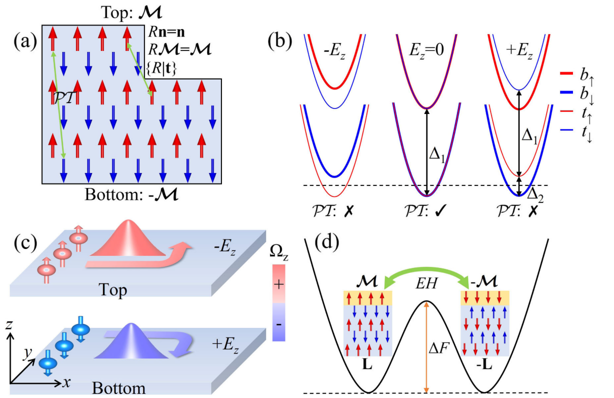

FIG. 1. (a) Illustration of roughness-robust surface magnetization $\mathcal{M}$ of ME AFMs. $\mathbf{n}$ is the surface normal. Red and blue arrows represent the magnetic moments. The point group operation R leaves both $\mathcal{M}$ and $\mathbf{n}$ invariant while the top and bottom layers are connected by $\mathcal{PT}$ symmetry. (b) Schematic spin splitting of surface bands and layer-locked band edges. $b_{\uparrow,\downarrow}$ ($t_{\uparrow,\downarrow}$) denotes the projection onto the bottom (top) surface states and $\uparrow, \downarrow$ is the spin index. The bands from bulk states are omitted for simplicity. Δ_1 (Δ_2) represents the magnitude of spin splitting by exchange field (electric field E_z). The $\mathcal{PT}$ symmetry is preserved ✓ (broken ✗) without (with) E_z and the dashed line denotes the position of Fermi energy. (c) Illustration of layer-locked Berry curvature Ω_z and layer Hall effect for positive and negative E_z. (d) Switching between two magnetic domain states by the combined E and H fields. ΔF denotes the energy barrier separating the two AFM domains.

[35–38]. By applying E_z, the surface bands are spin splitting due to $\mathcal{PT}$ symmetry broken and the spin-split magnitude is $\Delta_2 \propto E_z$, as illustrated in Fig. 1(b). Usually, the magnitude of Δ_1 is significantly larger than that of Δ_2 [32–34]; the band edge is thus contributed by either $b_\downarrow$ ($+E_z$) or $t_\uparrow$ ($-E_z$), resulting in the layer-locked spin-polarized band edges. Importantly, the Berry curvature becomes nonzero and layer-locked under finite E_z, thereby ensuring the layer Hall effect, as illustrated in Fig. 1(c). We see that the electrons from top and bottom layers deflect in opposite directions due to the opposite Berry curvatures Ω_z.

Our aforementioned discussion on the layer Hall effect can be formulated by a single-particle Hamiltonian (within the single-orbital approximation) as

$$H = \frac{\hbar^2 k^2}{2m} + \eta\left[\mathbf{h}(\mathbf{k}) \cdot \sigma - \frac{\Delta_1}{2}\mathbf{m} \cdot \sigma + \frac{\Delta_2}{2}\right], \qquad (1)$$

where the first term is the kinetic energy, the second term is the spin-orbit coupling (SOC), the third term is the exchange term due to $\mathcal{M}$, and the fourth term arises from the applied electric field. In Eq. (1), $\mathbf{h}(\mathbf{k}) = (h_x, h_y, h_z)$ characterizes the spin-orbit field defined in $\mathbf{k}$ space and can be determined by using the method of invariants [39–44], $\sigma = (\sigma_x, \sigma_y, \sigma_z)$ is the Pauli spin vector, and $\mathbf{m}$ is a unit vector of $\mathcal{M}$. $\eta = +1$ (-1) selects the top (bottom) layer. In

TABLE I. The MPGs for the (001) plane of several ME AFMs and the symmetry allowed Hamiltonian $\mathbf{h}(\mathbf{k})\cdot\sigma - \Delta_1/2\mathbf{m}\cdot\sigma$ (linear order in k) terms. λ represents the SOC parameter while Δ characterizes the Zeeman spin splitting. The symbol ✓ (✗) denotes the symmetry allowed (forbidden) Berry curvature. For each bulk MPG, the corresponding (001) plane MPG is obtained by gathering the symmetry operations that preserve the surface normal z being perpendicular to the (001) plane.

Bulk MPG	MPG for (001) plane	$\mathbf{h}(\mathbf{k})\cdot\sigma - \Delta_1/2\mathbf{m}\cdot\sigma$
$m'm'm'$	$m'm'2$ (✓)	$\lambda_{xy}k_x\sigma_y + \lambda_{yx}k_y\sigma_x - \Delta_z/2\sigma_z$
$mm'm$	$mm'2'$ (✗)	$\lambda_{xy}k_x\sigma_y + \lambda_{yx}k_y\sigma_x - \Delta_x/2\sigma_x$
$m'mm$	$m'm2'$ (✗)	$\lambda_{xy}k_x\sigma_y + \lambda_{yx}k_y\sigma_x - \Delta_y/2\sigma_y$
$4/m'$	4 (✓)	$\lambda_{xy}(k_x\sigma_y - k_y\sigma_x) + \lambda_{xx}(k_x\sigma_x + k_y\sigma_y) - \Delta_z/2\sigma_z$
$4/m'm'm'$	$4m'm'$ (✓)	$\lambda_{xy}(k_x\sigma_y - k_y\sigma_x) - \Delta_z/2\sigma_z$
$\bar{3}'$	3 (✓)	$\lambda_{xy}(k_x\sigma_y - k_y\sigma_x) + \lambda_{xx}(k_x\sigma_x + k_y\sigma_y) - \Delta_z/2\sigma_z$
$\bar{3}'m'1$	$3m'1$ (✓)	$\lambda_{xy}(k_x\sigma_y - k_y\sigma_x) - \Delta_z/2\sigma_z$
$\bar{3}'1m'$	$31m'$ (✓)	$\lambda_{xy}(k_x\sigma_y - k_y\sigma_x) - \Delta_z/2\sigma_z$
$6/m'$	6 (✓)	$\lambda_{xy}(k_x\sigma_y - k_y\sigma_x) + \lambda_{xx}(k_x\sigma_x + k_y\sigma_y) - \Delta_z/2\sigma_z$
$6/m'm'm'$	$6m'm'$ (✓)	$\lambda_{xy}(k_x\sigma_y - k_y\sigma_x) - \Delta_z/2\sigma_z$
$m'\bar{3}'$	$m'm'2$ (✓)	$\lambda_{xy}k_x\sigma_y + \lambda_{yx}k_y\sigma_x - \Delta_z/2\sigma_z$
$m'\bar{3}'m'$	$4m'm'$ (✓)	$\lambda_{xy}(k_x\sigma_y - k_y\sigma_x) - \Delta_z/2\sigma_z$

Eq. (1), the coupling between top and bottom layers is ignored by assuming large film thickness. Table I summarizes the symmetry allowed $\mathbf{h}(\mathbf{k})\cdot\sigma - (\Delta_1/2)\mathbf{m}\cdot\sigma$ terms for the (001) plane of several magnetic point groups (MPGs) of ME AFMs. Here, we list only the results for the (001) plane and the complete list is given in the Supplemental Material Table, Sec. II [45]. As an illustration, we consider $\mathbf{m}$ along z and h_z being negligible as compared to Δ_1. Then, the eigenvalues $\varepsilon_k^{\eta,\pm}$ and Berry curvature $\Omega_z^{\eta,\pm}$ are given by

$$\varepsilon_k^{\eta,\pm} = \frac{\hbar^2 k^2}{2m} + \eta\left(\frac{\Delta_2}{2} \pm \sqrt{h_x^2 + h_y^2 + \frac{\Delta_1^2}{4}}\right), \qquad (2)$$

and

$$\Omega_z^{\eta,\pm} = \mp \frac{\eta\Delta_1}{4(h_x^2 + h_y^2 + \Delta_1^2/4)^{3/2}}\left(\frac{\partial h_x}{\partial k_x}\frac{\partial h_y}{\partial k_y} - \frac{\partial h_x}{\partial k_y}\frac{\partial h_y}{\partial k_x}\right). \qquad (3)$$

From Eqs. (2) and (3), the total Berry curvature is zero when $E_z = 0$ and the polarity of Ω_z is controlled by the signs of Δ_1 and E_z, suggesting electrically switchable layer-locked Berry curvature.

Another point worth noticing is that the sign of $\mathcal{M}$ is uniquely linked to the Néel vector $\mathbf{L}$ in ME AFMs. This is due to the fact that $\mathcal{M}$ arises from one AFM sublattice and $\mathbf{L}$ is proportional to the difference of total magnetic moments between AFM sublattices [24–27]. $\mathcal{M}$ and $\mathbf{L}$ in ME AFMs are switchable by a combination of applied electric $\mathbf{E}$ and magnetic $\mathbf{H}$ fields [24–26], which paves the way for the ME manipulation of $\mathbf{L}$. We recall that there exists a free energy term $F(\mathbf{E},\mathbf{H}) = -\alpha_{ij}E_iH_j$ $(i,j = x, y, z)$ for centrosymmetric ME AFMs [28], where α_{ij} is the ME tensor. This term suggests a preferred magnetic domain state after annealing in a combination of $\mathbf{E}$ and $\mathbf{H}$ fields, called "magnetoelectric annealing" [25]. As sketched in Fig. 1(d), the two single domain states have opposite $\mathcal{M}$ and $\mathbf{L}$, which is, in principle, switched provided that $2\alpha_{ij}E_iH_j$ is larger than ΔF. Moreover, the large α_{ij} is favorable to reduce the required critical fields. The calculated longitudinal ME coupling coefficient for bulk Cr_2O_3 is $\alpha_{zz} = 0.002$ ps/m [60]. Such EH switching of $\mathcal{M}$ and $\mathbf{L}$ has been unanimously verified by the exchange bias switching in the CoPd/Cr_2O_3(0001) heterostructure [25].

Layer-locked band edges in the Cr_2O_3 *film*—Having demonstrated the layer Hall effect based on symmetry analysis, we next exemplify this in the prototypical Cr_2O_3 film. Bulk Cr_2O_3 (MPG $\bar{3}'m'$) has high Néel temperature ($T_N \approx 307$ K) [8,25] and large ME coupling [57,60,61]. Figure 2(a) shows the atomic structure of Cr_2O_3(0001) film composed of 6 and 12 atomic layers of O and Cr, respectively, and the surface is terminated by a single layer of Cr atoms, which has the lowest surface energy [62]. The magnetic moments of Cr atoms are aligned parallel in the (0001) plane and antiparallel along the [0001] direction. An electric field E_z is applied along the z direction (c axis) to engineer the electronic structures and Berry curvatures. Without E_z, the bands are doubly degenerate as enforced by $\mathcal{PT}$ symmetry. Under finite E_z, as shown in Figs. 2(b) and 2(c), the bands are spin splitting due to $\mathcal{PT}$ symmetry broken. Orbital projected band structures indicate that the band edges are dominantly contributed by the surface Cr atoms. Specially, spin up and down band edges are contributed by bottom ($b_\uparrow$) and top ($t_\downarrow$) Cr atoms, respectively, which is consistent with the surface magnetization orientations. We see that the layer-locked band edges are achieved in Cr_2O_3 film by E_z, and intriguingly, the spin

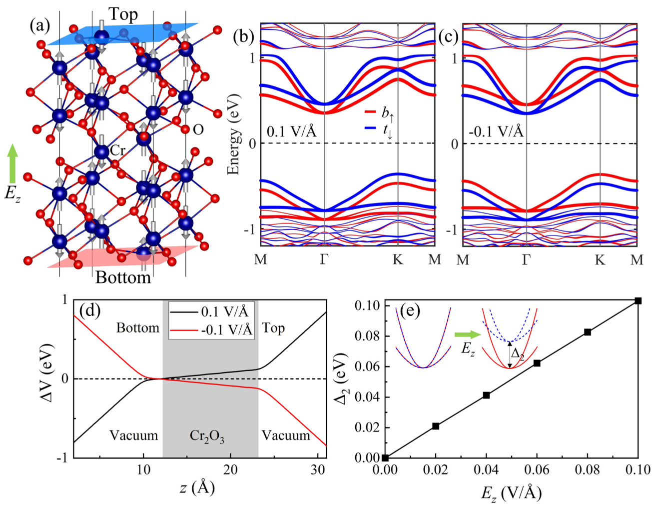

FIG. 2. (a) Atomic structure of Cr_2O_3 film. E_z denotes the applied electric field. Gray arrows denote the magnetic moments. Spin and layer projected band structure with (b) positive and (c) negative E_z ($E_z = 0.1$ V/Å) without SOC. (d) Electrostatic potential profile ΔV along the z direction. Here the sawtooth type ΔV near boundary is not shown. (e) Spin-split energy Δ_2 as a function of E_z. Inset: sketch of E_z-induced spin splitting near conduction bands.

polarization around the band edges is electrically switchable. This is due to the electrostatic effect [63], namely a potential difference between top and bottom layers is built and reversible by E_z, thereby interchanges the roles of spin up and down electrons around band edges, as seen from Fig. 2(d). Figure 2(e) shows the magnitude of spin splitting Δ_2 as a function of E_z. As expected, Δ_2 shows linearly dependence on E_z.

Layer Hall effect in the Cr_2O_3 *film*—Having demonstrated the layer-locked spin-polarized band edges by E_z, we next move to the Berry curvature engineering by E_z. Figure 3(a) shows the anomalous Hall conductivity σ_{xy} as a function of Fermi energy for different E_z. As consistent with the above symmetry analysis, σ_{xy} is zero (finite) without (with) E_z and is enhanced slightly with increasing E_z. Importantly, the polarity of σ_{xy} is fully switched when E_z is reversed (e.g., from 0.1 V/Å to −0.1 V/Å). This is due to the fact that the spin polarization is switchable by E_z as demonstrated in Figs. 2(b) and 2(c). It is to be noted that the possible defects or disorder may result in the uncompensated magnetization in Cr_2O_3 film, which naturally breaks the $\mathcal{PT}$ symmetry and gives rise to an AHE. However, as demonstrated in Supplemental Material, Sec. III [45], the defects have negligible effect on σ_{xy} under finite E_z. Figure 3(b) shows σ_{xy} as a function of $\mathbf{L}$ orientation θ (in x-z plane). We see that σ_{xy} shows a 2π periodic dependence on θ and satisfies $\sigma_{xy}(\theta) = -\sigma_{xy}(\theta + \pi)$ ($\mathcal{T}$-odd constraint). Interestingly, the $\mathbf{L}$ orientation dependence of nonlinear Hall conductivity for certain AFMs exhibits the similar behavior [16,17]. However, the layer Hall effect represents the first-order response to the electric field, being entirely different from the nonlinear Hall effect [12–17]. To further understand σ_{xy}, it is helpful to analyze the momentum-resolved total

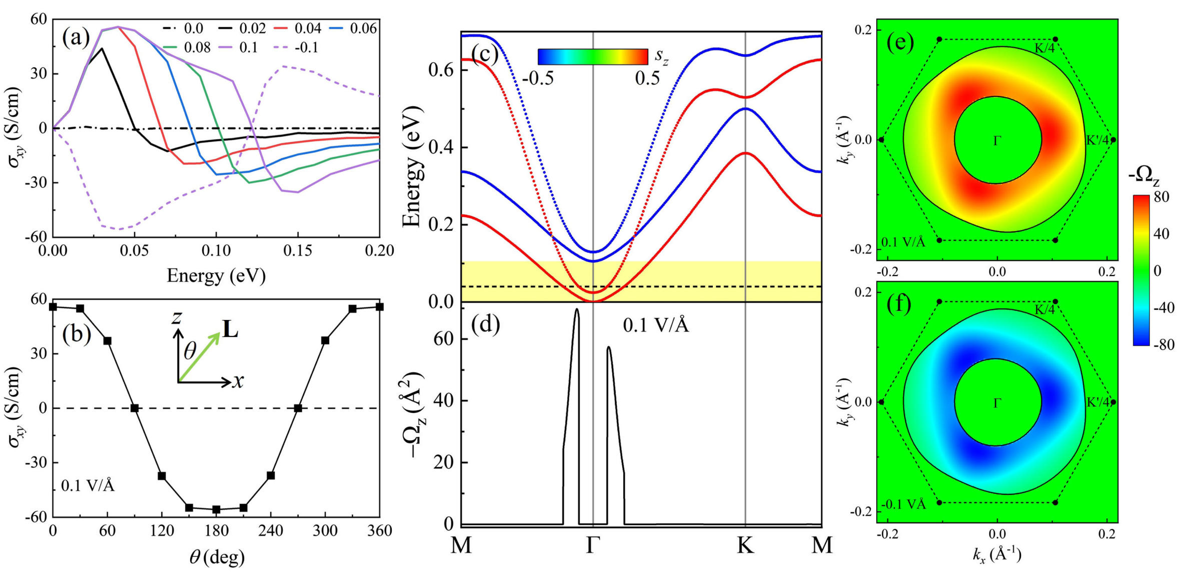

FIG. 3. (a) Anomalous Hall conductivity σ_{xy} of Cr_2O_3 film as a function of Fermi energy for different E_z. (b) σ_{xy} (Fermi energy of 40 meV) as a function of Néel vector $\mathbf{L}$ orientation θ (x-z plane, inset). (c) Spin projected band structure with SOC and magnetization along z axis. The color map quantifies the expectation value of the s_z component. The dashed line denotes the position of the Fermi energy. (d) Total Berry curvature $-\Omega_z(\mathbf{k})$ along symmetry lines $M - \Gamma - K - M$. $-\Omega_z(\mathbf{k})$ around Γ point in the first Brillouin zone for (e) $E_z = 0.1$ V/Å and (f) $E_z = -0.1$ V/Å. The solid lines represent the Fermi contours. The conduction band minimum has been aligned to zero.

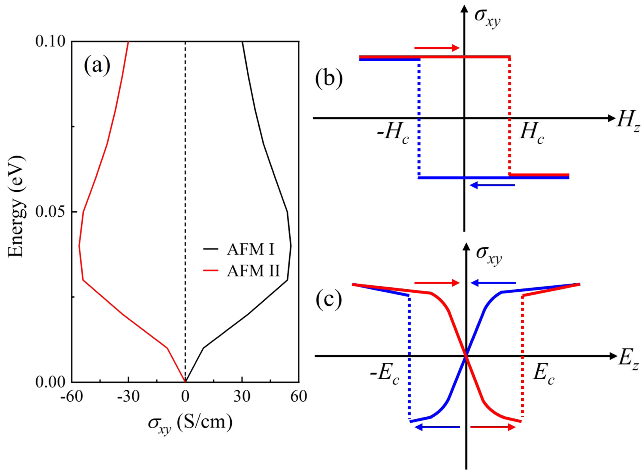

FIG. 4. (a) σ_{xy} of Cr_2O_3 film as a function of Fermi energy for AFM I and AFM II states with $E_z = 0.1$ V/Å. The conduction band minimum has been aligned to zero. (b) Schematic σ_{xy} versus the magnetic field H_z with a fixed electric field E_z. (c) Schematic σ_{xy} versus E_z with a fixed H_z. H_c and E_c denote the critical fields, at which $\mathcal{M}$ and $\mathbf{L}$ reverse.

Berry curvature $\Omega_z(\mathbf{k})$ since σ_{xy} arises from $\Omega_z(\mathbf{k})$ integrated in $\mathbf{k}$ space. Without loss of generality, we consider $E_z = 0.1$ V/Å and the Fermi energy of 40 meV in the following discussion. Figure 3(c) shows the spin s_z projected band structure with SOC. It is evident that the electrons are fully spin and layer polarized when the Fermi energy is within the energy window (highlighted in yellow). Figure 3(d) shows $-\Omega_z(\mathbf{k})$ along symmetry lines $M-\Gamma-K-M$. It is seen that $-\Omega_z(\mathbf{k})$ has large positive values near Γ point due to the small energy gap between occupied and unoccupied bands, which gives rise to Berry curvature peaks. Figures 3(e) and 3(f) show $-\Omega_z(\mathbf{k})$ around Γ point in the first Brillouin zone for $E_z = \pm 0.1$ V/Å. The large Berry curvatures occur in a trianglelike region around Γ point. Intriguingly, the polarity of $\Omega_z(\mathbf{k})$ is fully reversed by changing the direction of E_z. Thus, the bottom (top) layer sustains the AHE for positive (negative) E_z. We see that the electrically switchable layer Hall effect can be realized in Cr_2O_3 film, and more importantly, the layer Hall conductivity depends sensitively on $\mathbf{L}$ orientation, which provides an efficient route for $\mathbf{L}$ detection.

Layer Hall response to the combination of $\mathbf{E}$ *and* $\mathbf{H}$—As previously mentioned, the AFM domain state of ME AFMs can be switched by the combined electric and magnetic fields [see Fig. 1(d)]. As for Cr_2O_3, there are two degenerate AFM domain states, which are denoted as AFM I and AFM II. The switching between AFM I and AFM II states by the product E_zH_z has been confirmed experientially [25]. Since the switching from AFM I to AFM II or vice versa is equivalent to $\mathcal{T}$ operation, the polarity of σ_{xy} is expected to reverse. This is exactly what we find in density functional theory calculations, as shown in Fig. 4(a). Thus, the polarity of σ_{xy} is locked to AFM domain state and can be exploited to detect the Néel vector reversal. To illustrate this, Fig. 4(b) schematically shows σ_{xy} versus H_z with a fixed E_z. Starting from AFM I, σ_{xy} is positive. For the forward scan (red curve), when the product E_zH_z exceeds the energy barrier ΔF at the positive critical field H_c, the system enters into AFM II and σ_{xy} becomes negative. Similarly, for the backward scan (blue curve), the system changes from the AFM II to the AFM I state at the negative critical field $-H_c$. Figure 4(c) schematically shows σ_{xy} versus E_z with a fixed H_z, which reveals a butterflylike loop, as also has been observed in $MnBi_2Te_4$ film [18]. For the forward scan (red curve), starting from AFM I, σ_{xy} changes sign when E_z changes from negative to positive. At the positive E_c (e.g., $E_c = 2.6$ kV/mm [25] for a fixed magnetic field $\mu_0 H_z = 154$ mT), σ_{xy} changes sign for the second time due to the switching from AFM I to AFM II, indicative of Néel vector reversal. The backward scan (blue curve) reveals the similar behavior. Such E_z-dependent σ_{xy} paves the way for detecting the Néel vector reversal through layer Hall effect and provides new guidelines for the design of ME AFM memory device.

Discussion and summary—Our proposed layer Hall method provides electric means to detect the Néel vector, which is desirable for applications. This method is not limited by the wavelength of radiation and allows using it at sub 100 nm dimensions [4,10,11]. In contrast to the AMR [6,7] and *extrinsic* NHE [12,13] method, the layer Hall method is able to detect 180° reversal of the Néel vector. In contrast to the *intrinsic* NHE [15–17], layer Hall represents the first-order response to an electric field, which is favorable for experimental measurements.

The layer Hall detection is also applicable to other ME AFMs such as Fe_2TeO_6, $SrFe_2S_2O$, and Cr_2TeO_6 [45,58]. In addition, this approach can be applied to 2D Van der Waals exhibiting $\mathcal{PT}$ symmetry. For example, as we show in Supplemental Material, Figs. S2 and S3 [45], for monolayer MnSe [64] and two septuple-layer $MnBi_2Te_4$ [18], the Berry curvature can be efficiently engineered by an electric field and layer Hall conductivity depends sensitively on the Néel vector orientation. Moreover, the layer Hall detection is also applicable to certain ME AFMs with in-plane Néel vector. For example, as we show in Supplemental Material, Fig. S4 [45], for $SrFe_2S_2O(001)$ film [59], the layer Hall conductivity is sizable under an electric field and is electrically switchable.

In summary, we have proposed the layer Hall detection of the Néel vector in ME AFMs. Combining the robust surface magnetization and electrically spatial engineering of Berry curvature enables a sizable layer Hall signal, which depends sensitively on the Néel vector orientation. Combing the ME manipulation of the Néel vector ("write in") and the layer Hall detection scheme ("read off") in ME AFMs, it is promising to design all-electric control of antiferromagnetic memory devices. Looking forward, we hope that our work will enrich the techniques for the Néel vector detection, being beneficial for the design of antiferromagnetic spintronic devices.

Acknowledgments—This work was supported by the National Key Research and Development Program of China (Grant No. 2022YFA1402502), the National Natural Science Foundation of China (Grants No. 12274102, No. 52372004, No. 12274174), and the Fundamental Research Funds for the Central Universities (Grants No. FRFCU5710053421, No. HIT.OCEF.2023031). L. B. thanks the Vannevar Bush Faculty Fellowship Grant No. N00014-20-1C2834 from the Department of Defense and Grant No. DMR-1906383 from the National Science Foundation Q-AMASE-i Program (MonArk NSF Quantum Foundry). H. J. Z. acknowledges the support from Xiaomi YoungScholar project. E. Y. T. acknowledges support from the National Science Foundation through EPSCoR RII Track-1 program (Grant No. OIA-2044049). The atomic structures were produced using the VESTA software [65].

[1] T. Jungwirth, X. Marti, P. Wadley, and J. Wunderlich, Antiferromagnetic spintronics, Nat. Nanotechnol. **11**, 231 (2016).

[2] T. Jungwirth, J. Sinova, A. Manchon, X. Marti, J. Wunderlich, and C. Felser, The multiple directions of antiferromagnetic spintronics, Nat. Phys. **14**, 200 (2018).

[3] V. Baltz, A. Manchon, M. Tsoi, T. Moriyama, T. Ono, and Y. Tserkovnyak, Antiferromagnetic spintronics, Rev. Mod. Phys. **90**, 015005 (2018).

[4] P. Němec, M. Fiebig, T. Kampfrath, and A. V. Kimel, Antiferromagnetic opto-spintronics, Nat. Phys. **14**, 229 (2018).

[5] J. Han, R. Cheng, L. Liu, H. Ohno, and S. Fukami, Coherent antiferromagnetic spintronics, Nat. Mater. **22**, 684 (2023).

[6] P. Wadley, B. Howells, J. Železný, C. Andrews, V. Hills, R. P. Campion, V. Novák, K. Olejník, F. Maccherozzi, S. S. Dhesi *et al.*, Electrical switching of an antiferromagnet, Science **351**, 587 (2016).

[7] J. Železný, P. Wadley, K. Olejník, A. Hoffmann, and H. Ohno, Spin transport and spin torque in antiferromagnetic devices, Nat. Phys. **14**, 220 (2018).

[8] A. Mahmood, W. Echtenkamp, M. Street, J. L. Wang, S. Cao, T. Komesu, P. D. Dowben, P. Buragohain, H. Lu, A. Gruverman, A. Parthasarathy, S. Rakheja, and C. Binek, Voltage controlled Néel vector rotation in zero magnetic field, Nat. Commun. **12**, 1674 (2021).

[9] Y. H. Zhang, T. C. Chuang, D. Qu, and S. Y. Huang, Detection and manipulation of the antiferromagnetic Néel vector in Cr_2O_3, Phys. Rev. B **105**, 094442 (2022).

[10] M. J. Grzybowski, P. Wadley, K. W. Edmonds, R. Beardsley, V. Hills, R. P. Campion, B. L. Gallagher, J. S. Chauhan, V. Novak, T. Jungwirth, F. Maccherozzi, and S. S. Dhesi, Imaging current-induced switching of antiferromagnetic domains in CuMnAs, Phys. Rev. Lett. **118**, 057701 (2017).

[11] V. Saidl, P. Němec, P. Wadley, V. Hills, R. P. Campion, V. Novák, K. W. Edmonds, F. Maccherozzi, S. S. Dhesi, B. L. Gallagher *et al.*, Optical determination of the Néel vector in a CuMnAs thin-film antiferromagnet, Nat. Photonics **11**, 91 (2017).

[12] I. Sodemann and L. Fu, Quantum nonlinear Hall effect induced by berry curvature dipole in time-reversal invariant materials, Phys. Rev. Lett. **115**, 216806 (2015).

[13] D. F. Shao, S. H. Zhang, G. Gurung, W. Yang, and E. Y. Tsymbal, Nonlinear anomalous Hall effect for Néel vector detection, Phys. Rev. Lett. **124**, 067203 (2020).

[14] Z. Z. Du, H. Z. Lu, and X. C. Xie, Nonlinear Hall effects, Nat. Rev. Phys. **3**, 744 (2021).

[15] C. Wang, Y. Gao, and D. Xiao, Intrinsic nonlinear Hall effect in antiferromagnetic tetragonal CuMnAs, Phys. Rev. Lett. **127**, 277201 (2021).

[16] H. Liu, J. Zhao, Y.-X. Huang, W. Wu, X.-L. Sheng, C. Xiao, and S. A. Yang, Intrinsic second-order anomalous Hall effect and its application in compensated antiferromagnets, Phys. Rev. Lett. **127**, 277202 (2021).

[17] J. Wang, H. Zeng, W. Duan, and H. Huang, Intrinsic nonlinear Hall detection of the Néel vector for two-dimensional antiferromagnetic spintronics, Phys. Rev. Lett. **131**, 056401 (2023).

[18] A. Gao, Y. F. Liu, C. Hu, J. X. Qiu, C. Tzschaschel, B. Ghosh, S. C. Ho, D. Bérubé, R. Chen, H. Sun *et al.*, Layer Hall effect in a 2D topological axion antiferromagnet, Nature (London) **595**, 521 (2021).

[19] J. Železný, H. Gao, K. Výborný, J. Zemen, J. Mašek, A. Manchon, J. Wunderlich, J. Sinova, and T. Jungwirth, Relativistic Néel-order fields induced by electrical current in antiferromagnets, Phys. Rev. Lett. **113**, 157201 (2014).

[20] P. Wadley, S. Reimers, M. J. Grzybowski, C. Andrews, M. Wang, J. S. Chauhan, B. L. Gallagher, R. P. Campion, K. W. Edmonds, S. S. Dhesi, F. Maccherozzi, V. Novak, J. Wunderlich, and T. Jungwirth, Current polarity-dependent manipulation of antiferromagnetic domains, Nat. Nanotechnol. **13**, 362 (2018).

[21] M. Fiebig, Revival of the magnetoelectric effect, J. Phys. D **38**, R123 (2005).

[22] N. A. Spaldin and R. Ramesh, Advances in magnetoelectric multiferroics, Nat. Mater. **18**, 203 (2019).

[23] W. Eerenstein, N. D. Mathur, and J. F. Scott, Multiferroic and magnetoelectric materials, Nature (London) **442**, 759 (2006).

[24] A. F. Andreev, Macroscopic magnetic fields of antiferromagnets, J. Exp. Theor. Phys. Lett. **63**, 758 (1996).

[25] X. He, Y. Wang, N. Wu, A. N. Caruso, E. Vescovo, K. D. Belashchenko, P. A. Dowben, and C. Binek, Robust isothermal electric control of exchange bias at room temperature, Nat. Mater. **9**, 579 (2010).

[26] K. D. Belashchenko, Equilibrium magnetization at the boundary of a magnetoelectric antiferromagnet, Phys. Rev. Lett. **105**, 147204 (2010).

[27] S. F. Weber, A. Urru, S. Bhowal, C. Ederer, and N. A. Spaldin, Surface magnetization in antiferromagnets: Classification, example materials, and relation to magnetoelectric responses, Phys. Rev. X **14**, 021033 (2024).

[28] T. Martin and J. C. Anderson, Antiferromagnetic domain switching in Cr_2O_3, IEEE Trans. Magn. **2**, 446 (1966).

[29] R. Chen, H. P. Sun, M. Gu, C. B. Hua, Q. Liu, H. Z. Lu, and X. C. Xie, Layer Hall effect induced by hidden Berry curvature in antiferromagnetic insulators, Natl. Sci. Rev. **11**, nwac140 (2024).

[30] R. Peng, T. Zhang, Z. He, Q. Wu, Y. Dai, B. Huang, and Y. Ma, Intrinsic layer-polarized anomalous Hall effect in bilayer $MnBi_2Te_4$, Phys. Rev. B **107**, 085411 (2023).

[31] H. J. Zhao, X. Liu, Y. Wang, Y. Yang, L. Bellaiche, and Y. Ma, Zeeman effect in centrosymmetric antiferromagnetic semiconductors controlled by an electric field, Phys. Rev. Lett. **129**, 187602 (2022).

[32] H. Takenaka, S. Sandhoefner, A. A. Kovalev, and E. Y. Tsymbal, Magnetoelectric control of topological phases in graphene, Phys. Rev. B **100**, 125156 (2019).

[33] I. Žutić, A. Matos-Abiague, B. Scharf, H. Dery, and K. Belashchenko, Proximitized materials, Mater. Today **22**, 85 (2019).

[34] L. Tao and E. Y. Tsymbal, Insulator-to-conductor transition driven by the Rashba-Zeeman effect, npj Comput. Mater. **6**, 172 (2020).

[35] D. Xiao, M. C. Chang, and Q. Niu, Berry phase effects on electronic properties, Rev. Mod. Phys. **82**, 1959 (2010).

[36] L. Bellaiche, W. Ren, and S. Singh, Coupling of the angular momentum density with magnetic moments explains the intrinsic anomalous Hall effect, Phys. Rev. B **88**, 161102(R) (2013).

[37] R. Walter, M. Viret, S. Singh, and L. Bellaiche, Revisiting galvanomagnetic effects in conducting ferromagnets, J. Phys. Condens. Matter **26**, 432201 (2014).

[38] S. Du, P. Tang, J. Li, Z. Lin, Y. Xu, W. Duan, and A. Rubio, Berry curvature engineering by gating two-dimensional antiferromagnets, Phys. Rev. Res. **2**, 022025(R) (2020).

[39] L. L. Tao and E. Y. Tsymbal, Persistent spin texture enforced by symmetry, Nat. Commun. **9**, 2763 (2018).

[40] H. J. Zhao, H. Nakamura, R. Arras, C. Paillard, P. Chen, J. Gosteau, X. Li, Y. Yang, and L. Bellaiche, Purely cubic spin splittings with persistent spin textures, Phys. Rev. Lett. **125**, 216405 (2020).

[41] G. L. Bir and G. E. Pikus, *Symmetry and Strain-Induced Effects in Semiconductors* (Wiley, New York, 1974).

[42] L. L. Tao and E. Y. Tsymbal, Perspectives of spin-textured ferroelectrics, J. Phys. D **54**, 113001 (2021).

[43] X. Liu, H. J. Zhao, L. Bellaiche, and Y. Ma, Zeeman spin splittings with persistent spin textures in antiferromagnetic semiconductors, Phys. Rev. B **108**, 125108 (2023).

[44] L. L. Tao, J. Li, Y. Liu, X. Wang, Y. Sui, B. Song, M. Ye. Zhuravlev, and Q. Liu, Rashba-like spin splitting around non-time-reversal-invariant momenta, Phys. Rev. B **107**, 235138 (2023).

[45] See Supplemental Material at http://link.aps.org/supplemental/10.1103/PhysRevLett.133.096803, which includes Refs. [18,31,35,40,43,46–59], for information about computational details, complete list of magnetic point groups for different planes, effect of uncompensated magnetization, and layer Hall effect in 2D AFMs and the ME AFM with in-plane Néel vector.

[46] D. Vanderbilt, Soft self-consistent pseudopotentials in a generalized eigenvalue formalism, Phys. Rev. B **41**, 7892(R) (1990).

[47] P. Giannozzi, S. Baroni, N. Bonini, M. Calandra, R. Car, C. Cavazzoni, D. Ceresoli, G. L. Chiarotti, M. Cococcioni, I. Dabo *et al.*, QUANTUM ESPRESSO: A modular and open-source software project for quantum simulations of materials, J. Phys. Condens. Matter **21**, 395502 (2009).

[48] J. P. Perdew and A. Zunger, Self-interaction correction to density-functional approximations for many-electron systems, Phys. Rev. B **23**, 5048 (1981).

[49] N. Marzari and D. Vanderbilt, Maximally localized generalized Wannier functions for composite energy bands, Phys. Rev. B **56**, 12847 (1997).

[50] N. Marzari, A. A. Mostofi, J. R. Yates, I. Souza, and D. Vanderbilt, Maximally localized Wannier functions: Theory and applications, Rev. Mod. Phys. **84**, 1419 (2012).

[51] P. Giovanni, V. Vitale, R. Arita, S. Blügel, F. Freimuth, G. Géranton, M. Gibertini, D. Gresch, C. Johnson, T. Koretsune *et al.*, Wannier90 as a community code: New features and applications, J. Phys. Condens. Matter **32**, 165902 (2020).

[52] M. I. Aroyo, J. M. Perez-Mato, D. Orobengoa, E. Tasci, G. de la Flor, and A. Kirov, Crystallography online: Bilbao crystallographic server, Bulg Chem Commun **43**, 183 (2011).

[53] M. I. Aroyo, J. M. Perez-Mato, C. Capillas, E. Kroumova, S. Ivantchev, G. Madariaga, A. Kirov, and H. Wondratschek, Bilbao crystallographic server I: Databases and crystallographic computing programs, Z. Kristallogr. **221**, 15 (2006).

[54] M. I. Aroyo, A. Kirov, C. Capillas, J. M. Perez-Mato, and H. Wondratschek, Bilbao crystallographic server II: Representations of crystallographic point groups and space groups, Acta Crystallogr. Sect. A **62**, 115 (2006).

[55] Q. Wu, S. Zhang, H.-F. Song, M. Troyer, and A. A. Soluyanov, WANNIERTOOLS: An open-source software package for novel topological materials, Comput. Phys. Commun. **224**, 405 (2018).

[56] M. Buongiorno Nardelli, F. T. Cerasoli, M. Costa, S. Curtarolo, R. De Gennaro, M. Fornari, L. Liyanage, A. R. Supka, and H. Wang, PAOFLOW: A utility to construct and operate on *ab initio* Hamiltonians from the projections of electronic wavefunctions on atomic orbital bases, including characterization of topological materials, Comput. Mater. Sci. **143**, 462 (2018).

[57] J. Íñiguez, First-principles approach to lattice-mediated magnetoelectric effects, Phys. Rev. Lett. **101**, 117201 (2008).

[58] MAGNDATA, http://webbdcrista1.ehu.es/magndata.

[59] H. Guo, M.-T. Fernández-Díaz, A. C. Komarek, S. Huh, P. Adler, and M. Valldor, Long-range antiferromagnetic order on spin ladders $SrFe_2S_2O$ and $SrFe_2Se_2O$ as probed by neutron diffraction and Mössbauer spectroscopy, Eur. J. Inorg. Chem. **2017**, 3829 (2017).

[60] A. Malashevich, S. Coh, I. Souza, and D. Vanderbilt, Full magnetoelectric response of Cr_2O_3 from first principles, Phys. Rev. B **86**, 094430 (2012).

[61] E. Bousquet, N. A. Spaldin, and Kris T. Delaney, Unexpectedly large electronic contribution to linear magnetoelectricity, Phys. Rev. Lett. **106**, 107202 (2011).

[62] A. L. Wysocki, S. Shi, and K. D. Belashchenko, Microscopic origin of the structural phase transitions at the $Cr_2O_3(0001)$ surface, Phys. Rev. B **86**, 165443 (2012).

[63] S. Bhattacharjee, S. Singh, D. Wang, M. Viret, and L. Bellaiche, Prediction of novel interface-driven spintronic effects, J. Phys. Condens. Matter **26**, 315008 (2014).

[64] M. Aapro, Md. Nurul Huda, J. Karthikeyan, S. Kezilebieke, S. C. Ganguli, H. Gonzalez Herrero, X. Huang, P. Liljeroth, and H.-P. Komsa, Synthesis and properties of monolayer MnSe with unusual atomic structure and antiferromagnetic ordering, ACS Nano **15**, 13794 (2021).

[65] K. Momma and F. Izumi, VESTA 3 for three-dimensional visualization of crystal, volumetric and morphology data, J. Appl. Crystallogr. **44**, 1272 (2011).